# Interpolation of landslide movements to improve the accuracy of 4D geoelectrical monitoring

Author links open overlay panelSebastianUhlemann[ab]Paul B.Wilkinson[a]Jonathan E.Chambers[a]HansruediMaurer[b]Andrew J.Merritt[c]David A.Gunn[a]Philip I.Meldrum[a]
Show more

Highlights

- Investigation of 3D artefacts caused by electrode misplacements

- Interpolation of landslide movements to improve 4D resistivity monitoring

- Comparison of interpolators regarding their suitability for landslide investigation

## Abstract

Measurement sensors permanently installed on landslides will inevitably change their position over time due to mass movements. To interpret and correct the recorded data, these movements have to be determined. This is especially important in the case of geoelectrical monitoring, where incorrect sensor positions produce strong artefacts in the resulting resistivity models. They may obscure real changes, which could indicate triggering mechanisms for landslide failure or reactivation. In this paper we introduce a methodology to interpolate movements from a small set of sparsely distributed reference points to a larger set of electrode locations. Within this methodology we compare three interpolation techniques, i.e., a piecewise planar, bi-linear spline, and a kriging based interpolation scheme. The performance of these techniques is tested on a synthetic and a real-data example, showing a recovery rate of true movements to about 1% and 10% of the electrode spacing, respectively. The significance for applying the proposed methodology is demonstrated by inverse modelling of 4D electrical resistivity tomography data, where it is shown that by correcting for sensor movements corresponding artefacts can virtually be removed and true resistivity changes be imaged.

- **Previous** article in issue
- **Next** article in issue

## 1. Introduction

Landslides constitute one of the greatest natural hazards, causing tremendous damage every year and posing a significant risk to communities and infrastructure. Moreover, there is the potential that landslide occurrences may increase in the future due to changes in climate (Dijkstra and Dixon, 2010), the effects of which are yet to be investigated and understood. A major focus of international research is therefore to gain an improved understanding of triggering mechanisms and failure potentials, with the aim of developing landslide forecasting methodologies. Physical or process-based landslide models not only offer the best foundation to help in understanding the triggering mechanism, but also require a set of input parameters that have to be determined accurately to characterise the hydrological conditions of the slope (Dai et al., 2002, Dijkstra and Dixon, 2010).

Those data are obtained using techniques ranging from point sensors measuring, for example, moisture content or water potential, to volumetric monitoring of moisture movements using time-lapse electrical resistivity tomography (ERT). The latter is an approach that only very recently has become applied to studying landslides and unstable slopes in general (e.g., Gunn et al., 2014, Chambers et al., 2014, Supper et al., 2014). Due to its high sensitivity to lateral and temporal changes in moisture content, ERT is the geophysical technique that is most frequently applied to landslide investigations (Jongmans and Garambois, 2007, Jomard et al., 2007, Lebourg et al., 2010, Chambers et al., 2011).

However, due to the nature of ERT data interpretation, the locations of the individual electrodes within the ERT imaging array have to be known accurately to robustly interpret the measured data. In the case of a permanent installation on a landslide, electrode locations would have to be corrected for movements, which currently is not part of common processing workflows. Yet, misplacement of electrodes is known to cause severe artefacts in the resulting resistivity models (Zhou and Dahlin, 2003, Oldenborger et al., 2005, Szalai et al., 2008, Wilkinson et al., 2010), masking true resistivity variations due to changes in, e.g., moisture content. Changes in the separations of the electrodes change the measured potentials, which in turn affect the inverted resistivity models. Fig. 1 shows ratios of inverted resistivity models (commonly

used to highlight changes in resistivity) obtained from data acquired on a natural landslide in North Yorkshire, UK (i.e., Hollin Hill), before (March 2008) and after movement (March 2009). In Fig. 1a the electrode locations of 2008 were used for both the 2008 and 2009 resistivity data, while in Fig. 1b electrode locations measured in 2009 were used to invert the 2009 resistivity data. The difference between the two ratios (Fig. 1c) shows the effects of electrode misplacement on the resistivity ratio. In the area of movement (x < 10 m, 40 m < y < 80 m; shown by surface overlays with orange to black colours indicating progressively greater movement), the differences in resistivity ratio exhibit large variability with values ranging from − 0.6 to + 0.5. The largest differences occur close to the surface. These are positive (increased ratios) just beneath the northern part of the moving area (55 m < y < 80 m), and negative (decreased ratios) in the southern part. Below these near surface artefacts (> 2 m depth), deeper features of the opposite polarity are found extending to a depth of about 7 m below ground level (bgl). As resistivity ratios are commonly used to show changes in moisture conditions (Jomard et al., 2007, Chambers et al., 2014) which, in terms of landslide monitoring, can be used as proxy to slope stability (Lebourg et al., 2010), methodologies have to be developed to estimate electrode movements to minimise these artefacts and improve ERT monitoring applied to landslides.
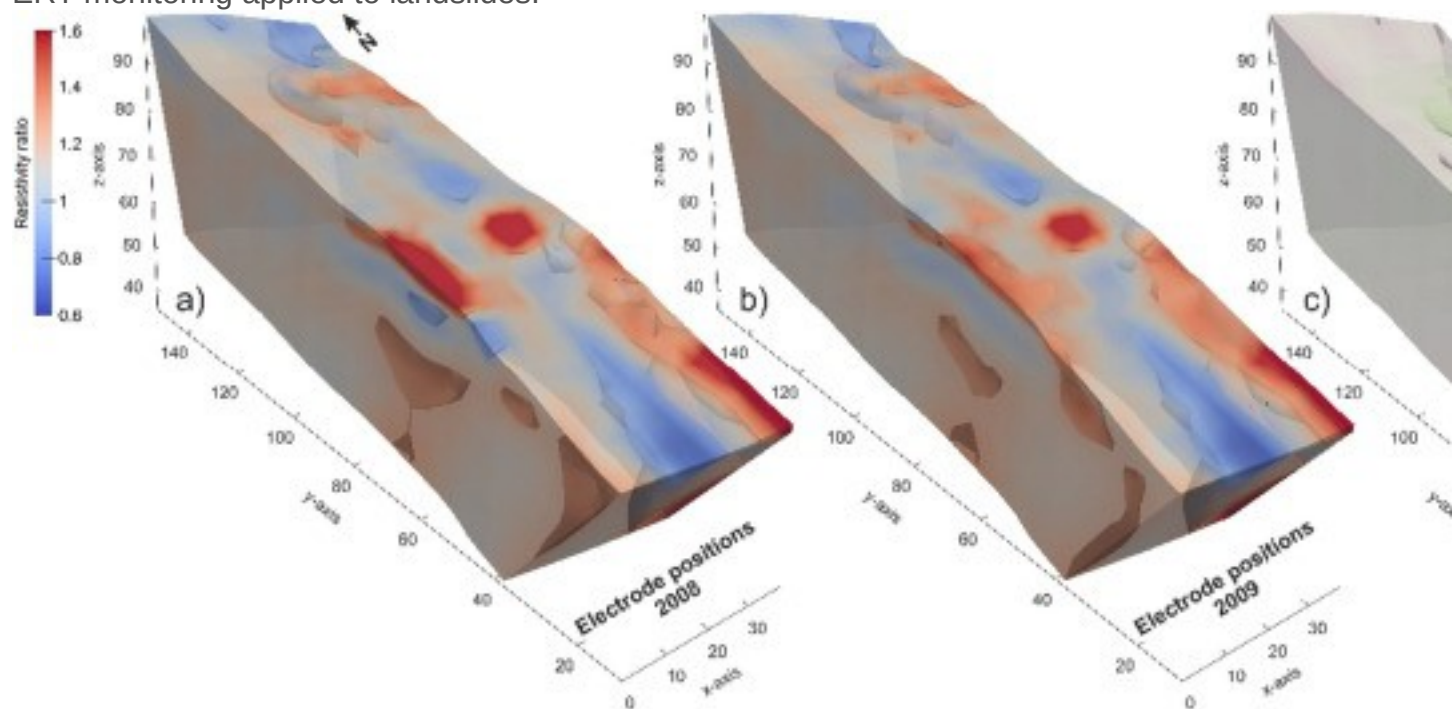


1. Download full-size image

Fig. 1. Resistivity ratios between measurements acquired on an active landslide from March 2008 and March 2009. Between these measurements electrodes in the western

part of the model ($x$ < 10 m) moved by up to 1.6 m. a) Shows the resistivity ratios for uncorrected electrode positions; in b) RTK-GPS measurements of the moved electrodes were included. The differences between the resistivity ratios (indicating the effect of electrode movement) are shown in c); artefacts in the resistivity ratios align with areas of severe movements.

While 2D ERT monitoring usually employs less than 100 electrodes, 3D ERT monitoring systems easily exceed this number. Manual monitoring of each electrode position with high spatial and temporal resolution is generally not practical due to the prohibitive time and number of site visits this would require. If the electrodes have been buried, re-surveying the electrodes is not possible at all. Therefore, we propose a methodology for which only a small set of reference points is monitored with high spatial accuracy (i.e., centimetric), using e.g., real-time kinematic (RTK) GPS surveying, with only limited temporal resolution. The movements of the reference points are then interpolated to a larger set of points of interest or to regular grids. In this study we compare the performance of three different interpolation techniques.

To validate the approach, we apply these techniques to 4D (i.e., 3D time-lapse) ERT monitoring problems, both on a synthetic model and a real installation on an active landslide. Techniques to estimate landslide movements are especially important for this application, since electrodes are usually buried underneath the surface. Therefore, repeated surveying of their locations is not possible. In the examples we interpolate the movements of reference points to a regular grid of points, where the ratio between known and interpolated points is about 1/5 and 1/4, respectively. Due to their complexity, including build-up of fissuring and sudden movements, interpolation of landslide movements can only deliver an estimate of true electrode displacements. However, for ERT measurements it is crucial to estimate these displacements to limit their effects on the resistivity data, inversions and subsequent interpretations.

## 2. Methodology

Discrete measurements of landslide movement are commonly used to derive velocities or displacements at the actual measurement points only (e.g., Mora et al., 2003, Corsini et al., 2005, Gance et al., 2014). However, for applications using a large set of points, e.g., ERT time-lapse imaging, monitoring of the movement of every single point is not feasible and a need arises to interpolate movement information of a sparse set of reference points (RP) onto a larger set of points of interest (PI) or regular grids, the positions of which are unknown.

Although this problem applies to a range of applications employing point sensors or sensor grids placed on a landslide, in this paper we will focus on 4D ERT. Note, however, that the methodology may be applicable for any other type of monitoring system.

A general procedure to monitor and interpolate landslide movement can be outlined as follows:

1.
Install/define points of interest (e.g., electrodes) $E_i$ and a set of reference points $R_j$.
2.
Survey initial locations $E_i(x,y,z)$ and $R_j(x,y,z)$ at the initial time $t_0$.
3.
Repeat survey of $R_j(x,y,z)$ at time $t_1$.
4.
Calculate directional movements $dx_j$, $dy_j$, $dz_j$ at each $R_j$-location.
5.
Interpolate the set of $dx$, $dy$, $dz$ to $E_i(x,y,z)$ using a suitable method.
6.
Update $E_i(x,y,z)$ by adding interpolated movement components $dx_i$, $dy_i$, $dz_i$.
7.
Repeat steps 3 to 6 for subsequent time steps.

After a certain time, and if the $E_i$ are accessible (e.g., not buried underneath the surface), the system can be recalibrated by surveying both the locations of $E_i$ and $R_j$. To obtain locations of $E_i$ for a time $t_k$ for which no actual $R_j$ data is available, an interpolation of $R_j$ to $t_k$ between the two adjacent measurements is proposed. Considering the type of movement observed at translation- or flow-dominated landslides in the UK (Uhlemann et al., in revision), a linear interpolation in time is usually sufficient.
A priori information, e.g., direct measurements of $E_i$ locations over time or areas where the $E_i$ are known to be static, can be included in the calculation of the updated $E_i$. This can be achieved by using this direct information instead of estimating the movements at the corresponding locations or by introduction of known boundaries of differential movement.
In the following we will discuss three different ways to interpolate the movements of the RPs to a larger set of PIs.

2.1. Piecewise planar interpolation (PP)

For this type of interpolation we use the mathematical definition that any point in a plane can be described by three non-collinear points spanning a basis. Here the three adjacent RPs are used to span the basis describing the location of a certain $E_i$ (see Fig. 2). The movement of these three points then describes the deformation of this plane. If we assume that the deformation caused by the landslide is rather smooth, we can use this relationship to derive a movement at the $E_i$.
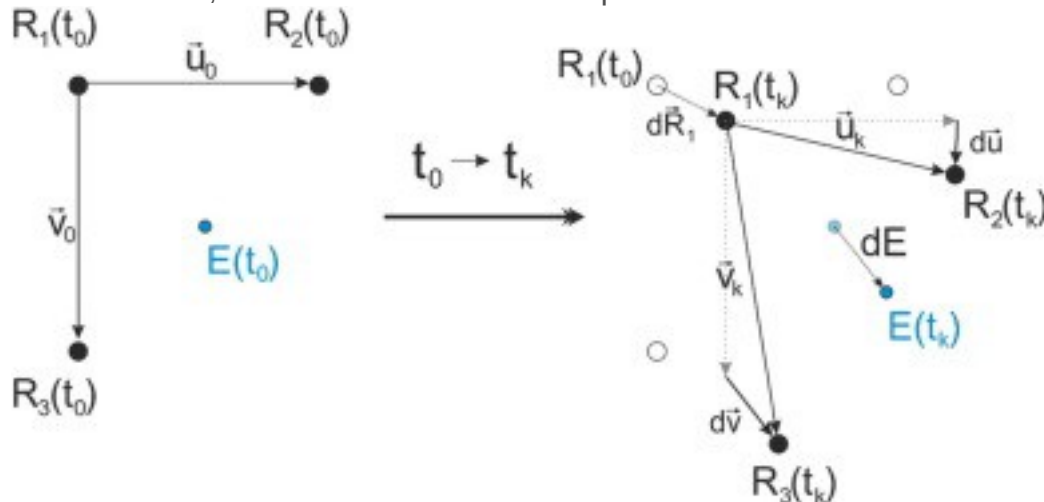


1. Download full-size image

Fig. 2. Schematic explanation of the piecewise planar interpolation scheme. The movement of the $E_i$ is defined by the change of the vectors $u$ and $v$.

According to Fig. 2 we can define the $E_i$ at an initial time $t_0$ as:

(1) $E_i t_0 = R_1 t_0 + s_u \cdot u \rightarrow 0 + s_v \cdot v \rightarrow 0 + s_n \cdot n \rightarrow 0$,

with $R_1(t_0)$ being the position of a "reference" marker at the initial time, and the last vector representing the unit normal vector to $u$ and $v$, defined as:

(2) $n \rightarrow 0 = u \rightarrow 0 \times v \rightarrow 0u \rightarrow 0 \times v \rightarrow 0$.

By including the normal vector we are able to describe electrode points which are located above or below the plane defined by the three reference points. This is a crucial prerequisite to account for topographic roughness which is typical for landslide morphology.

At time $t_0$ both, $E_i$ and the vectors between the RPs $u$ and $v$ are known and we can solve this equation to obtain the weights $s_u$, $s_n$, and $s_v$. These weights describe the contribution of each of the vectors to $E_i$ in relation to the $R_1$. If we assume that these weights also define the contribution that the movement of each RP will have on the movement of $E_i$ then these weights are constant in time and we can define the movement at $E_i$ as:

$$(3) \quad dE_i^{xyz} = d\vec{R_1} + s_u \cdot \vec{du} + s_v \cdot \vec{dv} + s_n \cdot \vec{dn},$$

where $dR_1$ describes the movement of $R_1$ from $t_0$ to $t_1$, and $du$, $dv$, and $dn$ the change of the vectors $u$, $v$, and $n$, respectively. By adding this movement to the initial $E_i$ an updated position can be determined and used for subsequent time steps.

## 2.2. Biharmonic spline interpolation (BS)

Biharmonic or multiquadric interpolation methods are specifically designed mathematical functions to interpolate data from a scattered set of RPs, and for topographical data sets in particular. The underlying theory is well understood and extensively described in the literature (e.g., [Hardy, 1971](), [Hardy, 1990](), [Sandwell, 1987]()). In brief, this method forms a global-interpolation scheme using linear combinations of biharmonic Green's functions ($\Phi$) centred on each RP ([Sandwell, 1987]()), minimising the curvature of the interpolator. For $N$ data points the interpolating surface for directional movements in $x$-direction (and $y$- and $z$-directions equally) is given by:

$$(4) \quad dx_{xy} = \sum_{j=1}^{N} \alpha_j \phi(x - x_j, y - y_j).$$

Here $\alpha_j$ represent the unknown contribution of each quadric function at the RPs to the interpolating surface. The biharmonic Green's function in two dimensions is defined as ([Sandwell, 1987]())

$$(5) \quad \phi(r) = r^2 (\ln r - 1),$$

with $r$ being a vector described by $r = (x - x_j, y - y_j)$.

Thus Eq. [(4)]() can be rewritten in matrix notation with the unknown $\alpha_j$ collated in $X$, the Green's functions in $A$, and the observed movements $dx$ in $B$, leading to $AX = B$ with the solution $X = A^{-1}B$. Hence, an inverse problem needs to be solved to obtain the contributions of each biharmonic Green's function centred at every RP. The resulting interpolation fits the data points exactly and provides a smooth surface with minimised curvature between measurement points for the estimation of movements at the $E_i$. This interpolation is performed in the same way for the directional movements along $y$- and $z$-axes, and, as outlined in the description of the general procedure, repeated for each time step $t_k$ between $t_0$ and a sought time $t_{end}$, with $E_i$ being updated after each iteration.

## 2.3. Kriging (KG)

Kriging is a well-established and widely used technique to find the best estimator of a spatially-dependent variable by considering the statistical characteristics of a known set of samples ([Matheron, 1971]()). In addition to a spatial estimation of a variable, kriging provides the uncertainty of this estimation. To obtain a kriging estimate, the variogram of

a sample data set has to be calculated and fitted by a correlation function. This relation is then used to calculate a spatial distribution of the sought variable ([Chilès and Delfiner, 2012](#)). The described workflow is shown for the $z$-component in [Fig. 3](#). The sample data set consists of the directional movements ($dx, dy, dz$) of each RP between its initial position and its position at the sought time $t_k$. This data is used to calculate a variogram for each component which is then fitted by a correlation function. In the case of landslide movement, the experimental data seems to be fitted best by exponential or cubic correlation functions (data in [Fig. 3](#)b has been fitted by a cubic function). The kriging estimates for the directional movements are sampled to a fine grid and interpolated onto the initial electrode position and the updated position for a time $t_k$ calculated. This procedure is then repeated for all following time steps until $t_{end}$ is reached.
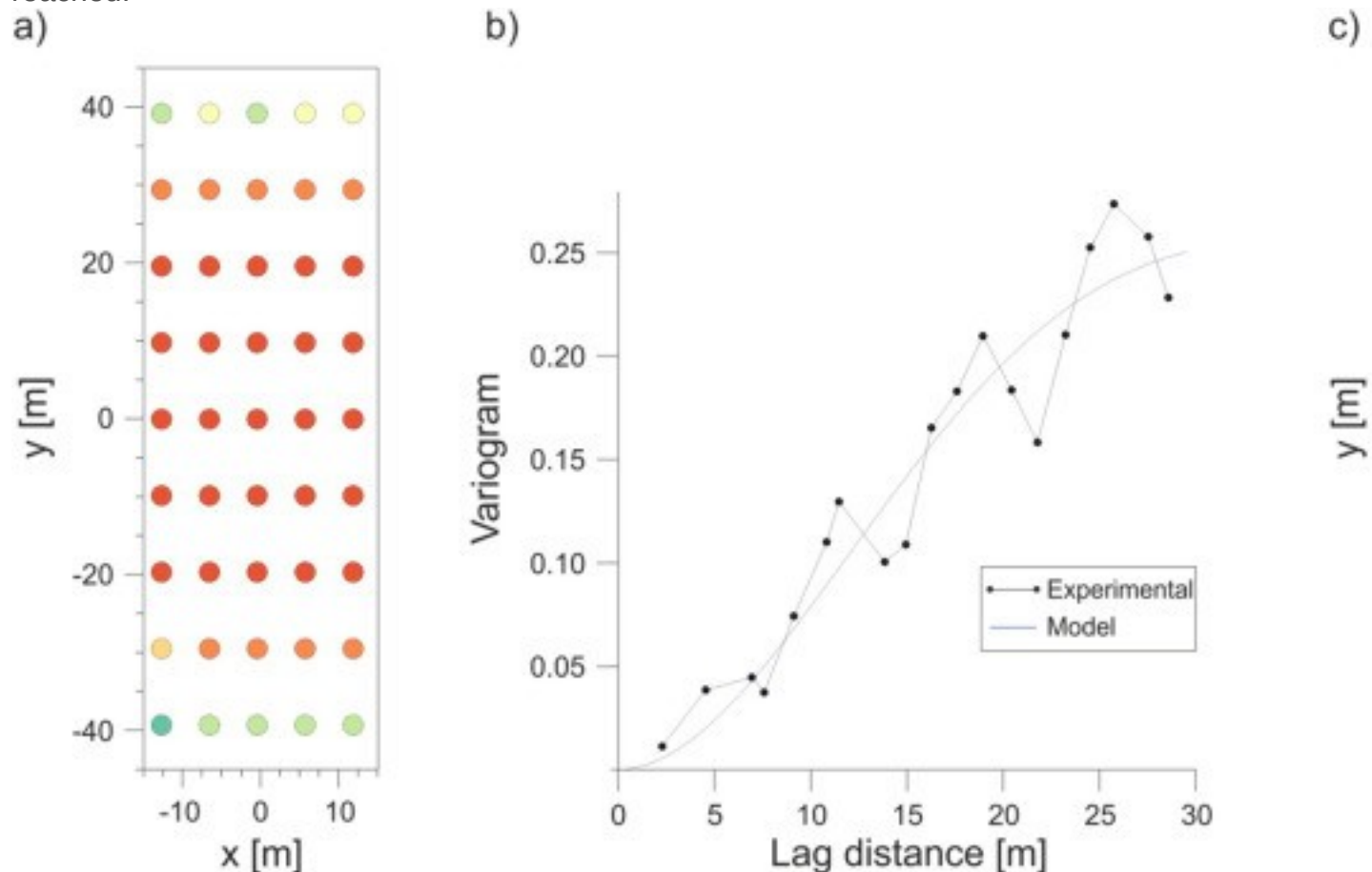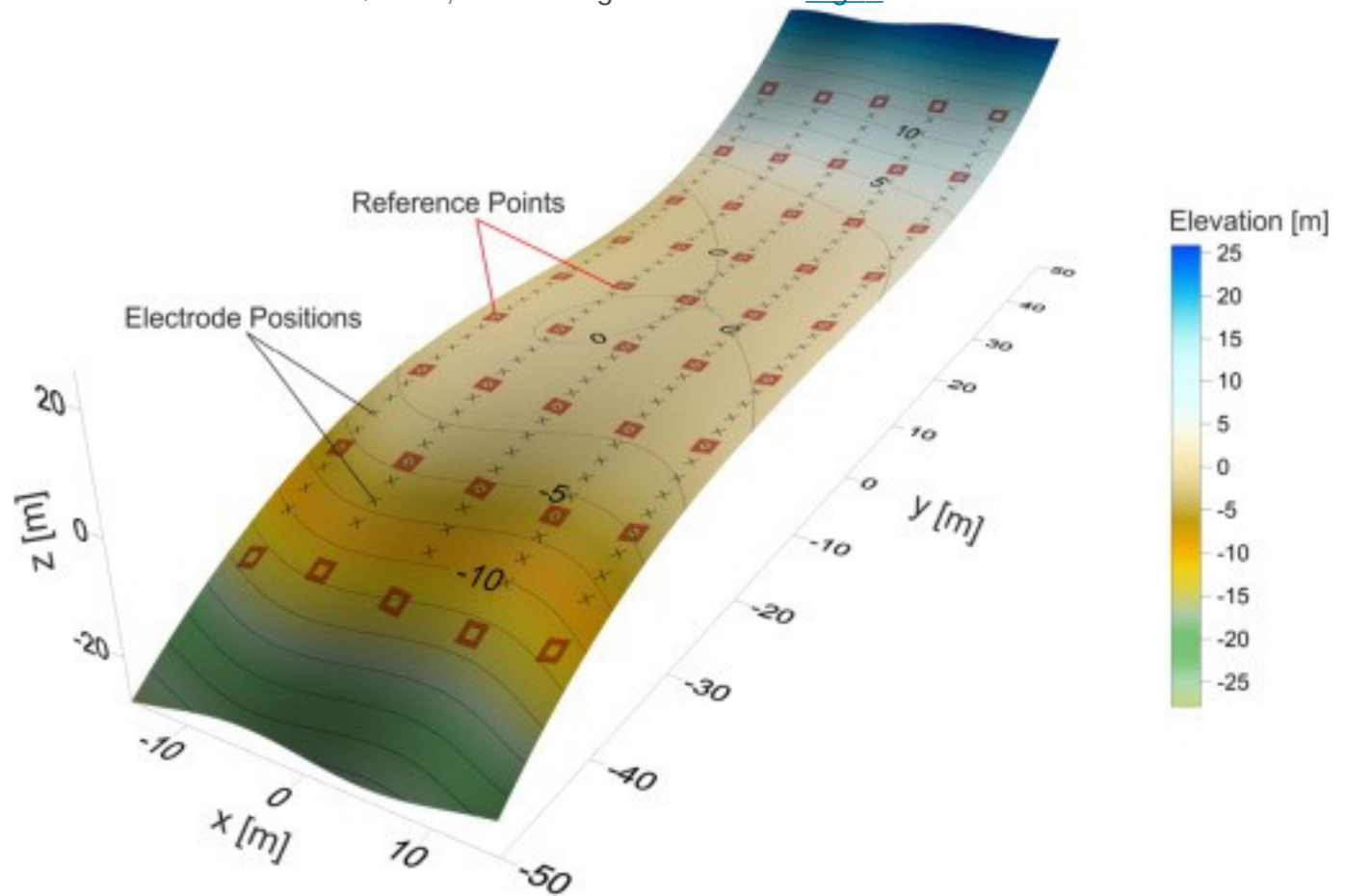


1. [Download full-size image](#)

Fig. 3. A kriging estimate (c) is derived from the interpolation of a sample data set (a) that follows a given statistical characterisation, i.e., the variogram of the data (b). This workflow is shown here for the $z$-component of the movement. The same procedure applies also to the $x$- and $y$-components.

## 3. Synthetic example

### 3.1. Model description

To test and compare the performance of these interpolation methods we set up a synthetic example, employing 190 PIs and 45 RPs. $E_i$ and $R_i$ are placed on a surface resembling realistic landslide morphology on a clayey slope, with changes in slope angle, and zones of depletion and accumulation. The initial $E_i$ and $R_j$ positions, as well as the surface on which $E_i$ and $R_j$ are moving are shown in <u>Fig. 4</u>.

Fig. 4. Initial $E_i$ (black crosses) and $R_i$ (red squares) positions located on a 3D surface resembling a realistic shallow clayey landslide morphology; colouring and isolines indicate elevation. $E_i$ and $R_i$ movements are defined by the gradient of the surface.

This example employs $E_i$ arranged in a regular grid, consisting of 5 parallel lines with 38 points per line. Along those lines their spacing is 2 m, while the spacing between two adjacent lines is 6.25 m. At each line 9 RPs are located with a spacing of 10 m. This results in a model dimension of 25 m-by-80 m. The maximum difference in elevation is

about 25 m, giving a mean slope ratio of 3.2, equivalent to a mean slope angle of about 17°.

Ground movements, and thus $E_i$ and $R_j$ movements, are modelled using the gradient of the topographic surface shown in Fig. 4. The movement of each point on the surface is defined to be opposite to the direction of the local gradient and proportional to its magnitude. The topography of the surface is assumed to remain constant over time. By multiple iterations a time series of $E_i$ and $R_j$ positions was created and the previously described interpolation methods were applied to it. Since $E_i$ and $R_j$ locations are known for each time step, this synthetic example provides the necessary information to quantitatively compare the estimated with true $E_i$ locations.

## 3.2. Results

Fig. 5 shows the non-linear displacement field for the time step at which the $E_i$ positions need to be determined by the use of the three techniques. While the movement in $x$-direction shows values ranging from − 0.6 m to 0.3 m, thus negative and positive changes along this axis, movements in $y$- and $z$-directions show larger amplitudes of up to − 3.0 m. Along the $z$-direction no positive changes can be observed (corresponding to up-slope movement, which was not deemed to be reasonable in this case). Areas towards the top and the bottom of the domain show the largest displacements, while areas in the middle ($y$ = − 10 m to + 10 m) show the smallest values.
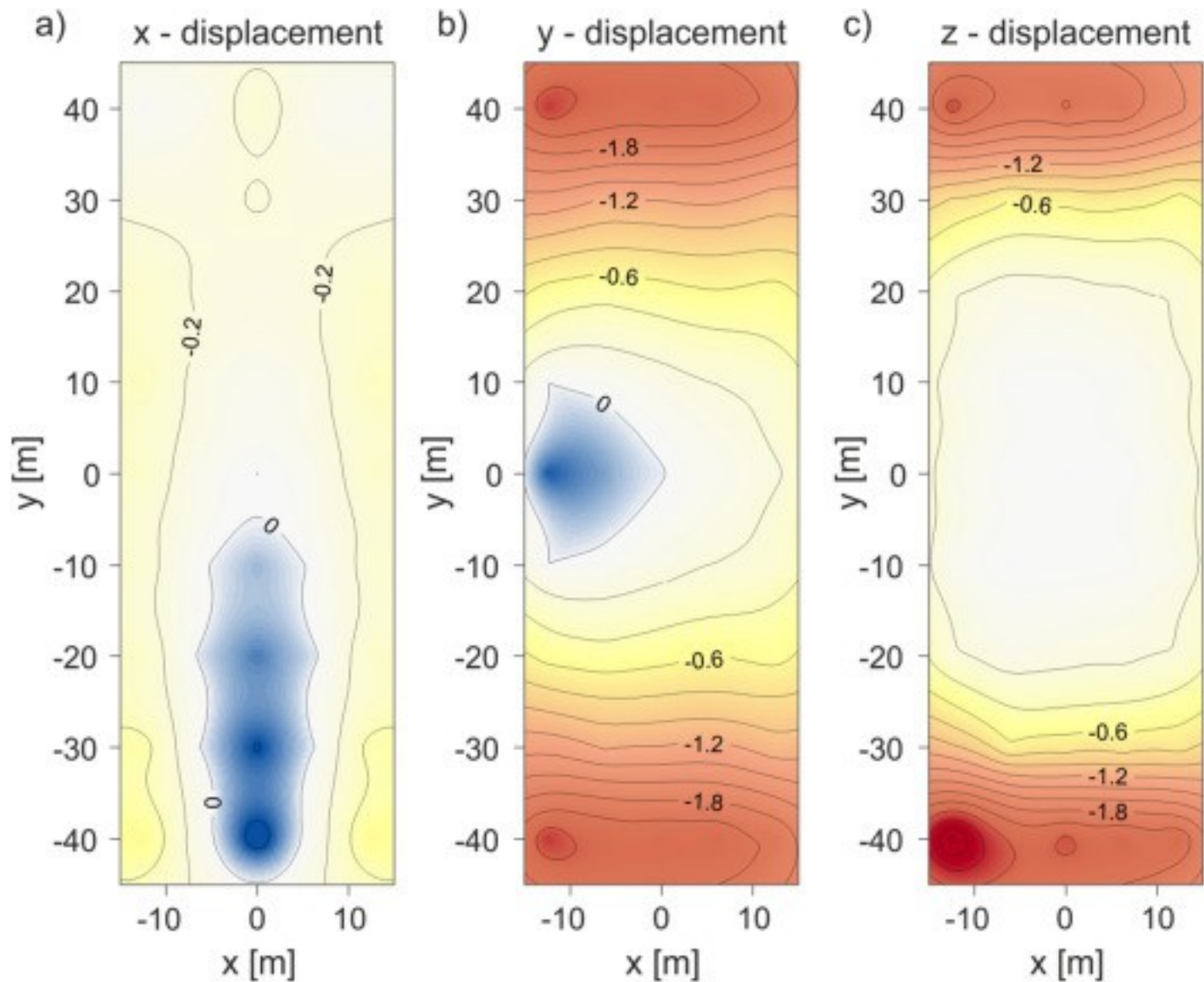
Fig. 5. Synthetic displacement field applied to the initial $E_i$ positions. The movement at each point is defined by the direction and magnitude of the local gradient.

Fig. 6 shows the misfits between the interpolated and the true $E_i$ for x-, y-, and z-components, as well as the absolute misfit. With a maximum misfit of less than 12.5% of the initial $E_i$ spacing (i.e., 2 m) all methods are shown to estimate movements reasonably well, but with clear differences in performance. BS provides the best estimation of electrode movements in all parts of the model. PP shows larger misfits, especially in the y- and z-components. The worst performance is given by KG, which clearly underestimates movements along the y- and z-axes.
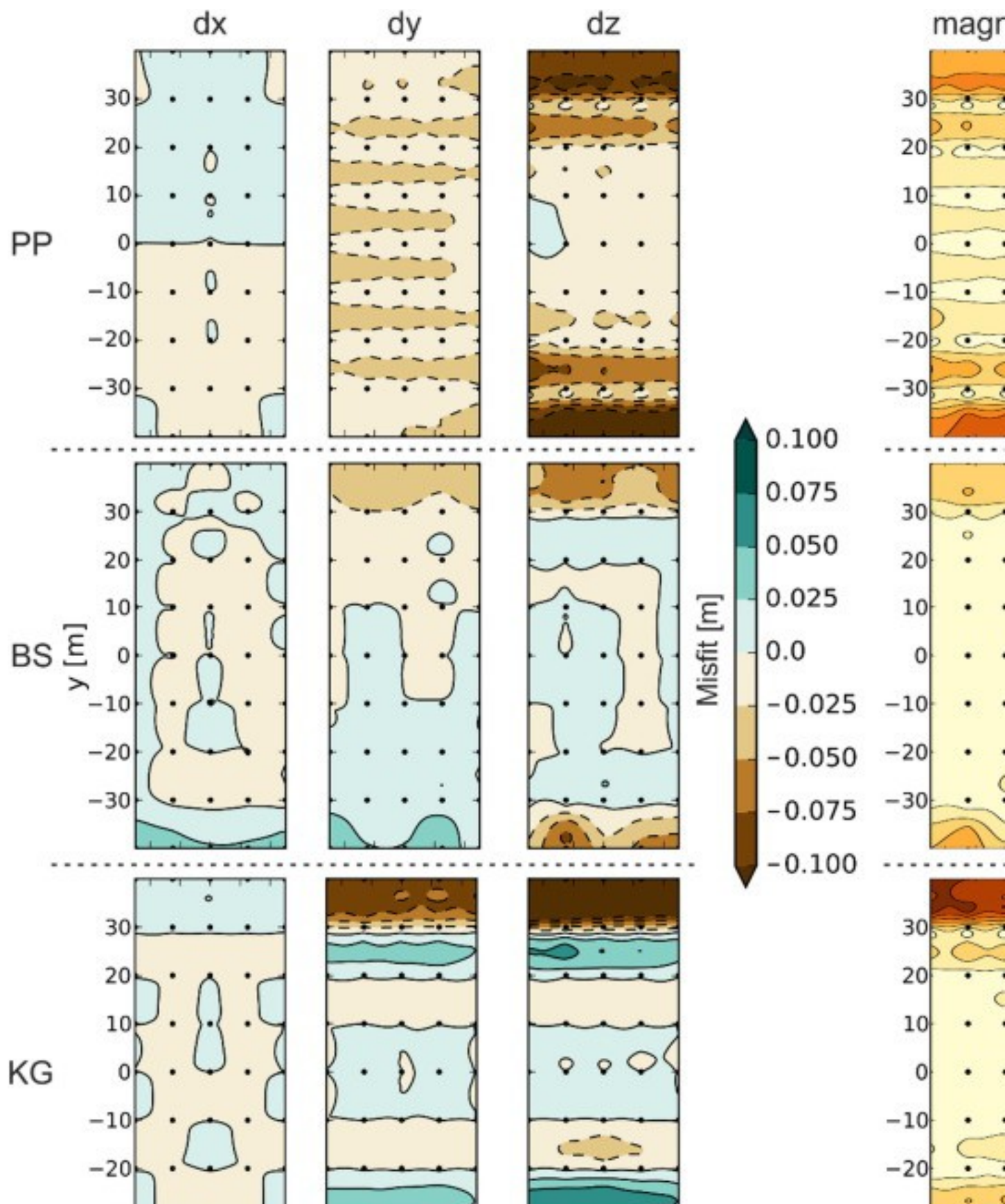
Fig. 6. Maps of misfit between true and interpolated electrode positions for *x*-, *y*-, *z*-components, and absolute misfit.

Throughout the model domain, areas of small movement magnitudes (Fig. 5) show also the smallest misfits for the *x*-component (< ± 0.05 m). All methods are able to estimate movements with an accuracy better than 10% of the actual movement rate. Areas characterised by large *y*-movements of up to 2.2 m are also characterised by large absolute misfits (< ± 0.10 m). PP shows a regular pattern of underestimation of movements, with largest misfits in regions between the $R_i$. In areas of large displacements (− 40 m < *y* < − 20 m, and 20 m < *y* < 40 m), positions are estimated with an accuracy better than 3% of the actual movement. This is not the case for areas of small or no displacements, where the misfit between true and estimated position may overwhelm the actual displacement. BS provides a comparable accuracy in areas of large displacement, but also better position estimation where only small displacements occur. It slightly underestimates movements in areas where the $R_i$ are moved closer together, while movements in areas where $R_j$ move apart are slightly overestimated. KG shows an alternation of over- and underestimation, where in areas of change in slope angle (− 30 m < *y* < − 20 m, and 20 m < *y* < 30 m) movements are overestimated, and in areas of large displacements (− 40 m < *y* < − 30 m, and 30 m < *y* < 40 m) movements are underestimated.

The same pattern can be observed for the KG misfit of the *z*-component, but with even higher amplitudes. BS, as for the other components, shows the smallest misfits (< 0.1 m) in the *z*-component. PP shows a similar misfit pattern in the *z*-component as for the *y*-component, with largest misfit between $R_j$ locations. For the model domain, the largest overall misfit of the *z*-component coincides with areas of largest displacements. This also propagates in the absolute misfit, which in these regions (− 40 m < *y* < − 20 m, and 20 m < *y* < 40 m) is up to 0.14 m (Table 1), equal to about 7% of the actual displacement. Better overall performance is achieved by BS, with a maximum total misfit of 0.09 m (better than 5% of the actual displacement). KG produces the worst fit, with misfits exceeding 0.20 m.

Table 1. Statistical comparison of the three different approaches. The discrepancy between true and estimated locations is given in metres.

| Offset [m] | Min | Max | Mean | RMS |
|---|---|---|---|---|
| PP | 0.000018 | 0.137 | 0.047 | 0.059 |
| BS | 0.000056 | 0.089 | 0.017 | 0.026 |
| KG | 0.000018 | 0.243 | 0.043 | 0.072 |

Table 1 shows some statistical values for the linear offset between estimated and true PI locations. Although PP and KG show the smallest offset, the mean offset of BS is at 0.017 m (= 0.85% of the initial electrode spacing) the smallest of the three techniques. KG includes the strongest over- or underestimations of the true movements and therefore exhibits the largest offset. PP and BS show comparable accuracy for the $x$- and $y$-components, but the BS estimation of $z$-displacements is superior. That BS is performing best on this example is also shown by the root-mean-square offset values (considering offset along all three axes), where this method has the smallest value at $RMS_{BS} = 0.026$ m compared to PP and KG at $RMS_{PP} = 0.059$ m and $RMS_{KG} = 0.072$ m, respectively.

Note that the KG results depend strongly on the accuracy of the correlation function with which the experimental variogram is fitted. Choosing a wrong type of function or parameters will inevitably lead to poor estimations of the PI movements. In addition, to calculate a meaningful variogram the sample data set has to have sufficient data points, which may limit the applicability of this method for field applications. We found that for the given dimensions and movement rates a set of at least 30 points is necessary to obtain a meaningful variogram and correlation function in turn.

In addition to these smooth interpolators, also nearest and natural neighbour type interpolators have been tested. The results (although not shown here) indicate a worse performance of these interpolation types. This can be attributed to the smooth nature of the synthetic example.

## 3.3. Effect on 3D inverse modelling

Movement of sensors deployed on a landslide will inevitably influence the interpretation of their measured data. Especially for ERT, accurate electrode positions have to be known to avoid artefacts in the data. This is shown best by the effects of wrong electrode positions on inverse modelling of the measured resistivity distribution (Wilkinson et al., 2010). Here, the electrode positions derived in the synthetic example will be used. Using COMSOL® Multiphysics we simulated the response of a homogeneous halfspace of $\rho = 100$ Ωm for the true electrode locations, i.e., after movement. The modelled data set comprised 4285 standard dipole–dipole measurements oriented along the $y$-axis and 4212 equatorial dipole–dipole measurements. Data including the different electrode positions were inverted using a smoothness-constrained least-squares inversion method, employing a L1-norm for both the data misfit and model roughness (Loke and Barker, 1996). The forward problem was

solved using a finite-element method, allowing the topography to be integrated into the model. Fig. 7 shows the inverted resistivity models. The model using the true positions indicates the accuracy of the inversion, with resistivity values ranging between 85 and 115 Ωm. The inverted model employing the initial electrode positions, i.e., without movement correction, highlights the necessity to correct electrode positions for movement. This model shows strong artefacts in the areas of movement, especially at top and bottom, but also throughout the model domain. The model resistivities range from 65 to 180 Ωm, showing resistivity changes which are larger than commonly observed by changes in, e.g., moisture content or salinity. The correlation coefficient between the two models of $R = 0.471$ highlights the strong disturbance of the resistivity distribution by using wrong electrode positions. Using the interpolation techniques these artefacts can be virtually removed. The resistivity model obtained using the PP estimated electrode positions shows a resistivity distribution that is very similar to the model using the true positions, proven by a correlation coefficient of $R = 0.997$.
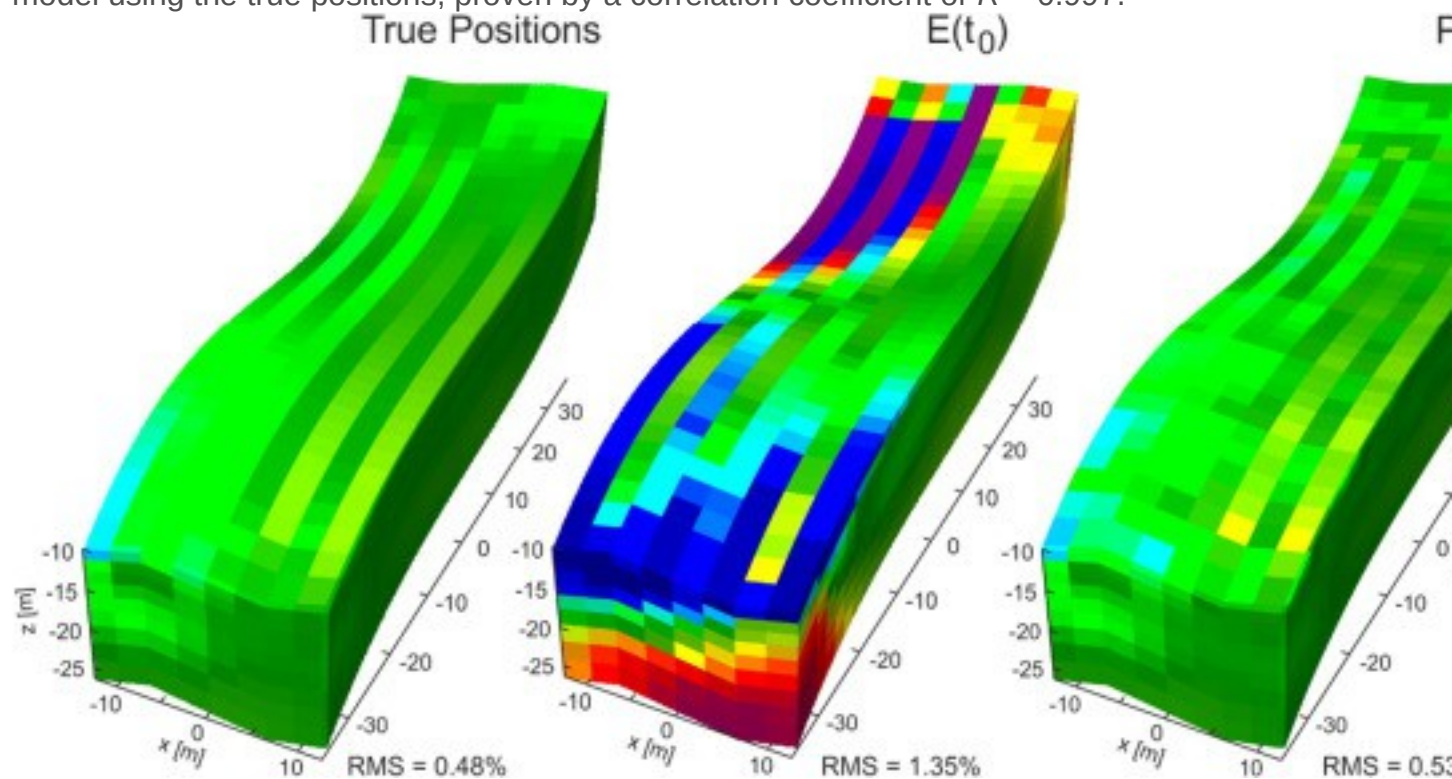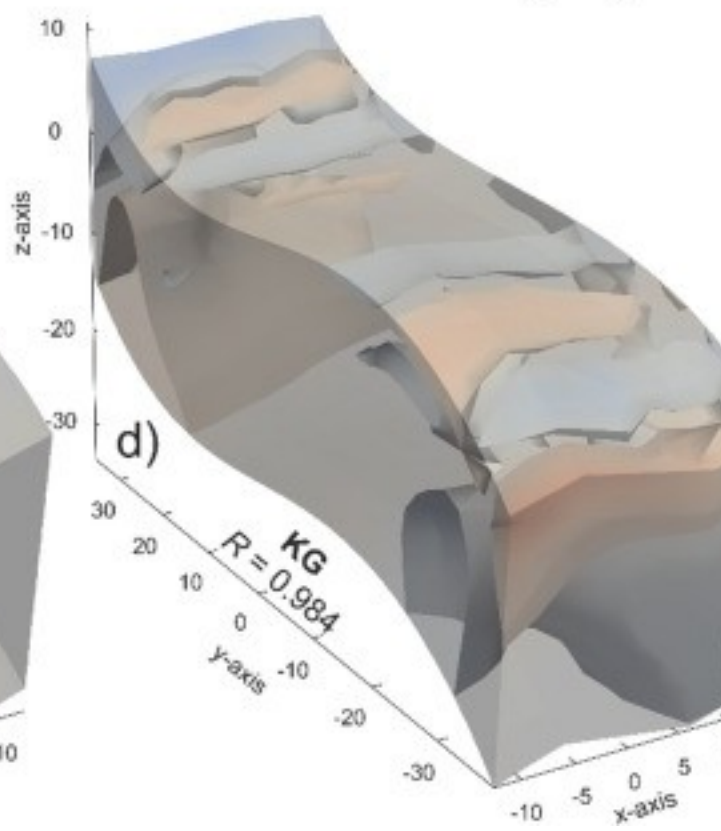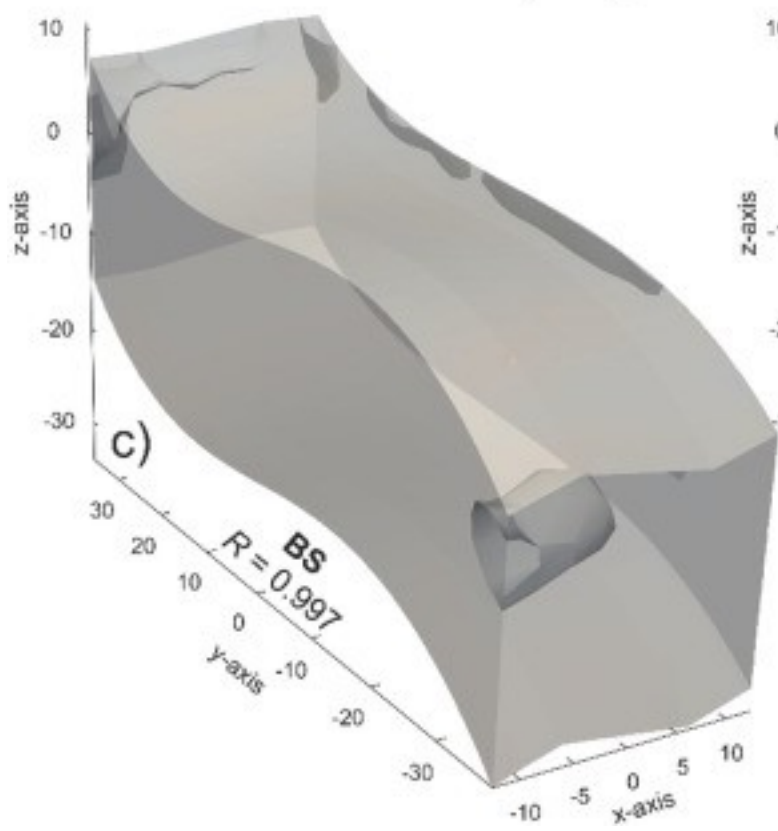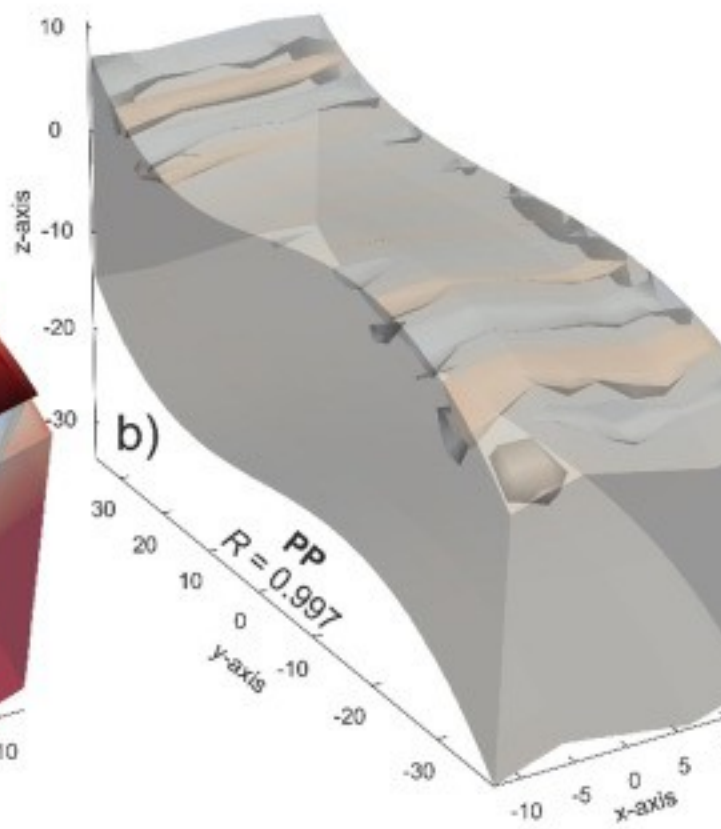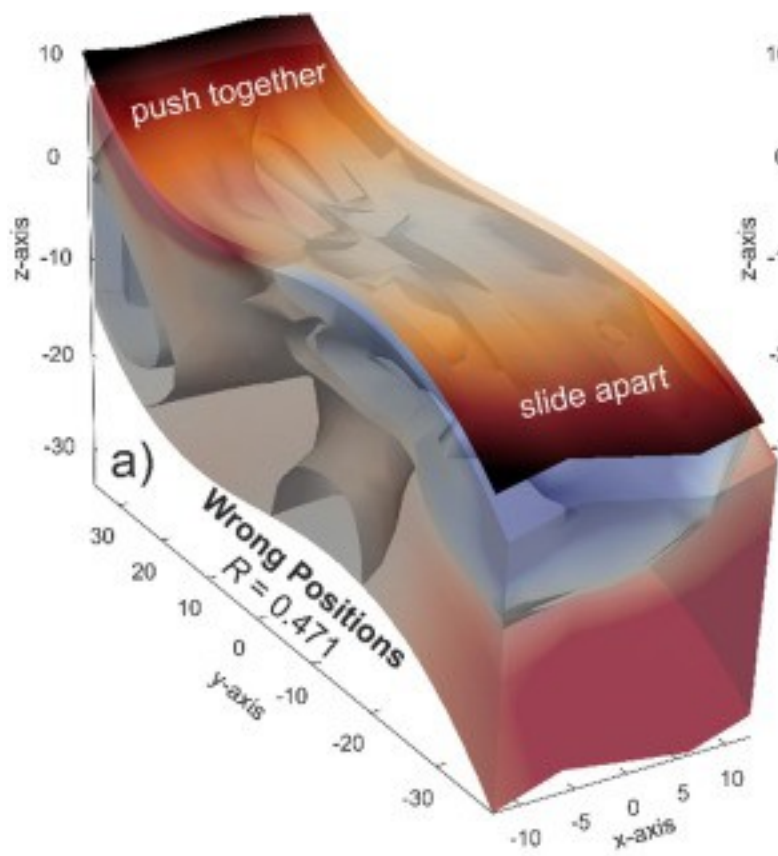


1. Download full-size image

Fig. 7. 3D Block models of inverted resistivity data employing (left) true, (middle) initial and (right) PP-interpolated electrode positions.

Fig. 8 shows the resistivity ratios of models using uncorrected and interpolated electrode locations to the model employing true positions, highlighting the artefacts caused by electrode misplacement. Red colours (i.e., values greater than 1) indicate

resistive anomalies, while blue colours (i.e., values lower than 1) indicate conductive anomalies. In the uncorrected case (Fig. 8a) electrode movements resulted in near-surface artefacts overestimating the resistivity at the top of the model ($y$ = 10 to 35 m) and underestimation between $y$ = − 25 m and − 5 m. These are the regions with the largest amplitude electrode displacements where spacing have been decreased or increased, respectively, due to different movement rates. Small deviations in electrode positioning are known to cause near-surface artefacts (Szalai et al., 2008). Here, where movements lead to electrode displacements of more than the initial electrode spacing, resistivity artefacts are also severe in deeper parts of the model. These deep artefacts are of different polarity than the corresponding near-surface features. The resistive anomaly in the upper part of the model, where electrodes move together, is underlain by a conductive anomaly. The conductive near-surface anomaly of the lower part of the model, where electrodes move apart, is underlain by a resistive anomaly. The amplitudes and depth of the near-surface artefacts correlate with the electrode displacement. At greater depths, artefacts are not necessarily constrained to movement areas, but can also be found away from these regions.

a) push together
slide apart
**Wrong Positions**
$R = 0.471$

b) **PP**
$R = 0.997$

c) **BS**
$R = 0.997$

d) **KG**
$R = 0.984$

Fig. 8. Resistivity ratios between resistivity models using a) initial (i.e., uncorrected), b) PP, c) BS, and d) KG interpolated electrode positions and the resistivity model employing true locations; the overlay in a) shows the absolute electrode movement. Isosurfaces show resistivity ratios of 1.02 (red) and 0.98 (blue), respectively. Note in the uncorrected case, areas where electrodes are pushed together show resistive anomalies, while areas of electrodes sliding apart are characterised by reduced resistivities. For each section the correlation coefficient between the corresponding resistivity model and the true model is given.

While the resistivity ratios range from 0.57 to 1.49 for the uncorrected model, correcting for electrode movements reduces this range considerably to values spanning from 0.95 to 1.04 for PP, and 0.94 to 1.03 for BS. For BS artefacts are virtually removed. In the case of PP and KG, the remaining artefacts correlate with the misfits between estimated and true electrode positions. For PP, these artefacts are constrained to the near-surface. Artefacts in KG still propagate into deeper layers, but amplitudes are significantly reduced, with resistivity ratios ranging from 0.85 to 1.08. This slightly worse result is highlighted by a lower correlation coefficient of $R = 0.984$, compared to $R = 0.997$ for both PP and BS. However, all interpolation methods are able to provide electrode positions with sufficient accuracy to remove artefacts in the inverted resistivity models, thus providing a methodology for robust ERT data processing and interpretation.

## 4. Real data example

Although the synthetic example helps to highlight the capabilities of the introduced methodology, it is a simplified and smoothed model of electrode movements compared to a real, natural landslide. Therefore, we have to test and judge the methodology applied to a real landslide problem.

To develop a better understanding of the precursors leading to first-time failure and reactivation of landslides, the British Geological Survey is operating an observatory on an active landslide in North Yorkshire, UK, acting as a representative example for landslides in Lias Group mudrocks. This group, the Whitby Mudstone Formation (WMF) in particular, shows one of the highest landslide densities in the UK (Chambers et al., 2011, Hobbs et al., 2012, Gunn et al., 2013). The observatory comprises 4D geoelectrical (i.e., ERT and self-potential monitoring), geotechnical (i.e., acoustic emission and inclinometer) and hydrological/environmental monitoring (i.e., weather station, soil moisture, soil temperature) (Dixon et al., 2010, Wilkinson et al.,

2010, Merritt et al., 2013). ERT monitoring at site is undertaken using a grid of electrodes attached to a BGS-designed ALERT system (Ogilvy et al., 2009, Wilkinson et al., 2010) for bi-daily observation of the 3D resistivity distribution of the landslide. Due to its location on an active, moving landslide, and the fact that misplaced electrodes can cause severe artefacts in resistivity imaging (Zhou and Dahlin, 2003, Wilkinson et al., 2010), the grid of electrodes will form a set of PIs in the following.

4.1. Site location and geological characterisation

The landslide observatory is located at Hollin Hill near the village of Terrington, North Yorkshire, UK. It is a south-facing hill slope used as pasture land for sheep with a mean slope angle of 12°. Geologically, the site comprises four formations of Lower and Middle Jurassic age. The hill is capped by the Dogger Formation (DGF), consisting of calcareous sandstone and ferruginous limestone, representing a potential aquifer overlying the WMF, which is the failing formation at site (Fig. 9). The WMF contains grey to dark grey mudstone and siltstone with scattered bands of calcareous and sideritic concretions (Chambers et al., 2011). It is underlain by the Staithes Sandstone Formation (SSF) consisting of ferruginous, micaceous siltstone with fine-grained sandstone and thin mudstone partings. This formation is highly bioturbated (Gaunt et al., 1980) and forms a well-drained loam soil, characteristic for the middle-part of the escarpment. At site, the WMF and SSF are highly weathered, showing low stiffness between 1–5 MPa (Gunn et al., 2013). The SSF overlies the Redcar Mudstone Formation (RMF). A spring line exists at the boundary of these two formations.

a)      b)
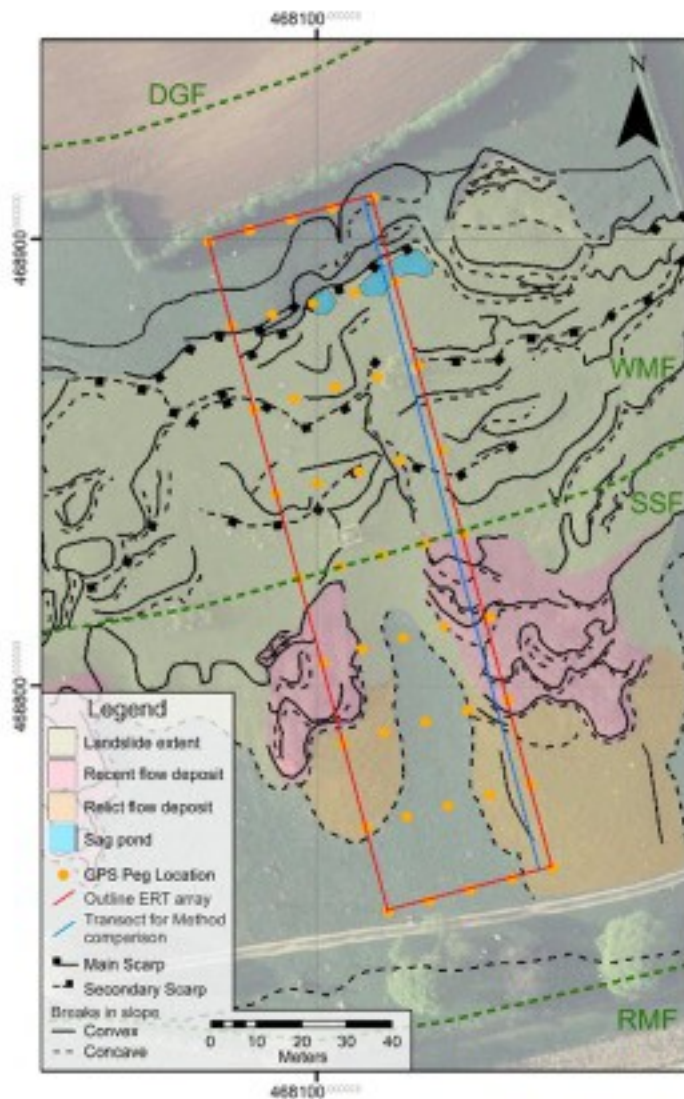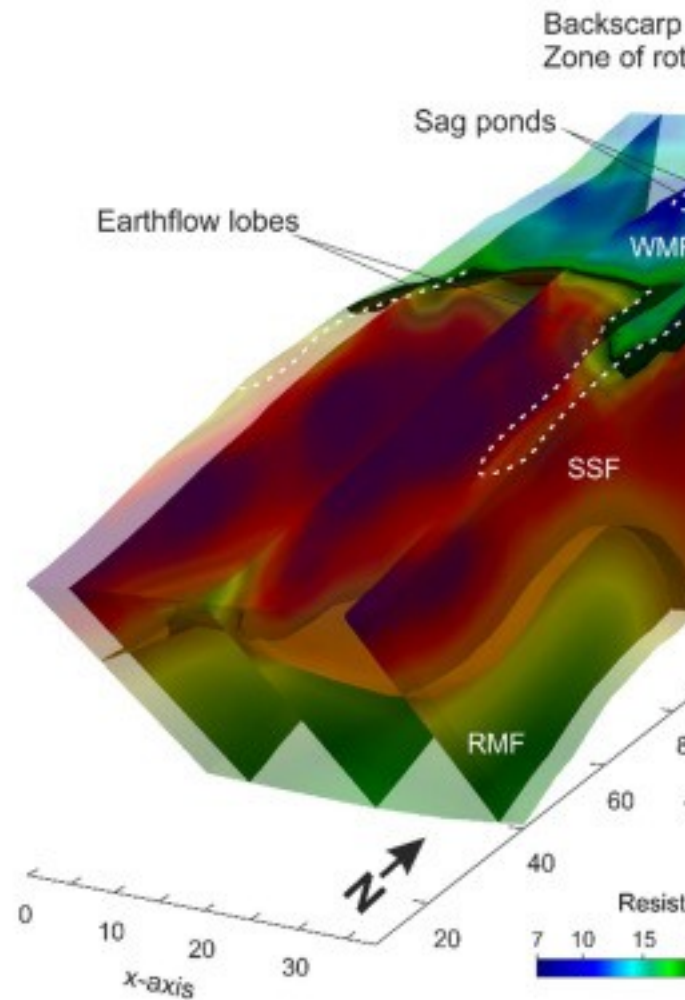
Fig. 9. a) Geomorphological map showing the main landslide features and the outline of the ERT monitoring area (adapted from Merritt et al. (2013)). b) Interpreted 3D resistivity model (resistivity and position data of March 2012); boundaries between WMF and SSF (postulated as being the sliding surface), and between SSF and RMF are highlighted.

Merritt et al. (2013) present a thorough geomorphological characterisation of the slope (see Fig. 9a). In brief, the top, northern part of the slope is characterised by the main scarp of the landslide showing rotational failure, with active shallow, and less-active, deeper-seated slumps. Further down the slope earth-flows have developed, where the WMF has slipped over the SSF, forming several lobes.

The main geological formations have successfully been imaged using 3D ERT (Fig. 9b). While the WMF and RMF are characterised by resistivities lower than 30 Ωm (governed

by their high clay content), the SSF shows higher resistivities ranging between 30 Ωm and 70 Ωm. Thus, the sliding surface, which is postulated to be the interface between SSF and WMF, can be extracted on the basis of the formation resistivities. The resistivity model outlines the extent of the earth flow lobes, both in the lateral and vertical dimensions. The benefit of applying resistivity tomography to landslide monitoring is its sensitivity to moisture content, which is, along with porosity and pore water resistivity, one of the main factors determining the formation resistivity (Archie, 1942). Since moisture content changes more rapidly than porosity and pore water resistivity, volumetric imaging of resistivity changes can provide useful proxy information to understand moisture content changes, thereby (1) helping to characterise the hydrological regime of the landslide, e.g., imaging of preferential flow-paths or zones of moisture discharge and accumulation, and (2) understanding the triggering mechanisms for landslide reactivation or first-time failure.

## 4.2. Movement monitoring and estimation

The 3D ERT monitoring set-up at Hollin Hill consists of a grid of 160 electrodes, arranged in 5 parallel lines with 32 electrodes spaced at 4.75 m intervals each, and inter-line spacing of 9.5 m. The line spacing being twice the electrode spacing forms a practical limit for maintaining resolution when combining linear array measurements for 3D ERT data inversion (Gharibi and Bentley, 2005). With this layout the ERT monitoring array covers an area of approximately 145 m × 38 m, equal to about 0.5 ha. The electrodes are buried about 10 cm beneath the surface to prevent damage from other activities or by animals at site. The initial electrode positions have been recorded in March 2008 when the monitoring setup was installed. Measurements are scheduled, conducted, and stored using the ALERT system. The measurement sequence employs conventional, cross-line and equatorial dipole–dipole measurements, including a full set of reciprocal measurements for data quality assessment.

Since the electrodes have no expression at the surface, a set of marker pegs has been installed to track the electrodes movements. Nine markers are installed along each of the five lines, with a spacing of about 17.5 m (see Fig. 9a). Every 1–2 months these markers are surveyed using a real-time kinematic GPS system with centimetric accuracy, providing a time-series of measurements building the basis for employing the introduced movement estimation procedure.

In spring 2013, the lower ($y = 0$ m to 80 m) and the uppermost ($y = 135$ m to 155 m) part of the eastern-most line were excavated and the electrode positions surveyed. Electrode positions of the western-most line that were subject to movement in 2008–

2009 were re-surveyed during each site visit after the installation. Thus offering a data set of true positions against which the estimated positions can be compared, about 5 years after their installation and various periods of active movement. Note that movements of the eastern lobe only commenced at the end of 2012, therefore true electrode locations were known until then. Fig. 10 shows the misfit between true and estimated electrode displacements of the eastern-most ERT line, interpolated from the marker movement using the three different schemes. Along this line, two regions with large soil movements exist. One is located at the upper, northern end of the slope (between $y = 135$ m and 150 m), another one further south between $y = 35$ m and 60 m. While the northern area shows mainly negative movement along the $y$-axis (i.e., downslope), the displacement in the southern part additionally shows negative movement along the $x$-axis, caused by the lobe progressing into a gully structure. The survey of the electrode positions indicated a maximum movement of 3.5 m, with a mean of 1.65 m at this line.

With all interpolators electrode positions could be estimated with an accuracy better than 1.3 m for each component, thus the general trend and scale are interpolated well. As for the synthetic example, movement rates in the $x$-direction are smaller than in the $y$- and $z$-directions, and therefore misfits are smaller along this direction as well; for all interpolators and throughout the slope the $x$-misfit stays below 0.5 m (< 5.5% of the line spacing). Within the flow-dominant domain (electrode numbers 1–11) movement patterns are comparably complex, with markers showing contrasting movement directions and scales, i.e., eastward followed by westward movement, and strong movements of up to 3.5 m adjacent to regions of no movement. The soil movement on this lobe is characterised by several shallow flowing regimes (Uhlemann et al., in revision), thus increasing the complexity of the movement. This is shown by misfits of the $y$- and $z$-components of up to 1.0 m, i.e., at electrode number 7, situated in a region where movement changes from negative to positive $x$-wards movement. The comparably larger misfits along the $z$-axis can be attributed to the rough and discontinuous surface deformation along the lobes. The misfits of electrodes 12 and 13 in the rotation-dominated part of the landslide can be attributed to a change in movement type between the adjacent markers; the upper marker was placed in the slipped part, while the lower marker was set in the zone of material accumulation. None of the methods, however, were able to recover a strong contrast in movement between electrodes located at $y = 33$ m and 34.75 m. While the latter is located at the tip of the lobe of the earth flow, the first is placed on the non-moving SSF and eventually became covered with flow material. As the non-moving zones are known, they have been

included in the estimation and electrodes within those zones stay constant (highlighted areas in Fig. 10). This highlights that the estimation quality of the presented interpolation techniques depends on the sampling density (spatially and temporal) and relation to the degree of complexity of the soil movements at a research site. While highly heterogeneous movement will require higher sampling densities, rather homogeneous movement will require significantly fewer sampling points.
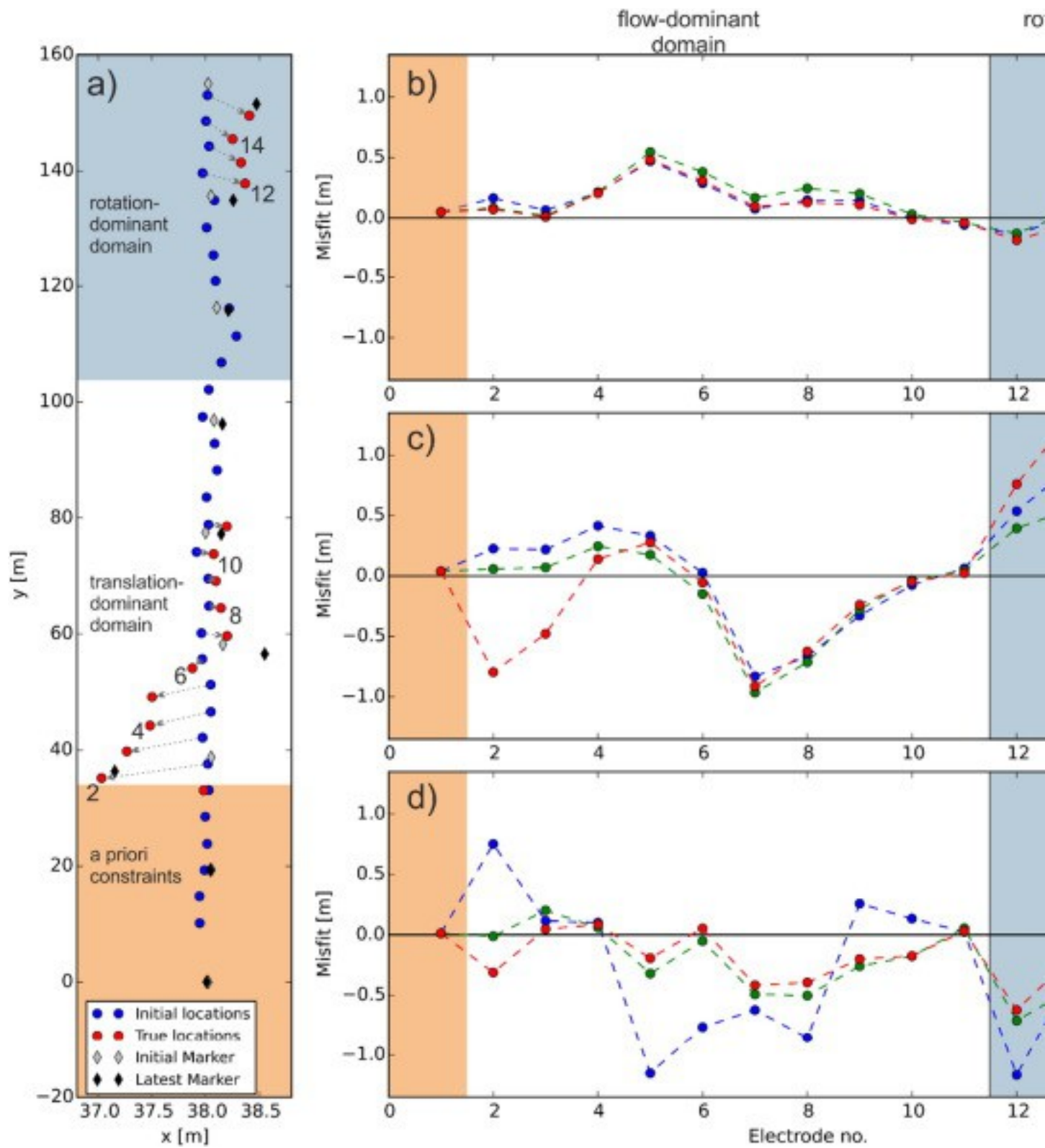
Fig. 10. a) Map showing initial and RTK-GPS measured electrode positions (i.e., true locations) from spring 2013 (annotated numbers indicate the electrode number as

plotted in b–d). b)–d) Show misfit between interpolated and true electrode positions for *x*, *y*, and *z*-components.

Although the non-moving zones have been used as a priori information, due to the highly heterogeneous movements between markers at *y* = 35 m and 56.5 m the maximum offsets between estimated and true positions remain high, with values of 0.88 m, 0.98 m, and 1.30 m for PP, BS, and KG, respectively (see Table 2). Also in terms of a root-mean-square offset, KG shows the largest value ($RMS_{KG}$ = 0.64 m), thus highlighting that a purely statistical approach fails to provide a good estimate of the complex deformations on landslide, which are recovered to a better degree by methods which are based on a more physical approach of deformations of planes or splines caused by "forces" acting on them.

Table 2. Statistical comparison of the remaining offsets between true and estimated electrode locations.

| Offset [m] | Min | Max | Mean | RMS |
|---|---|---|---|---|
| PP | 0.063 | 0.883 | 0.416 | 0.487 |
| BS | 0.045 | 0.980 | 0.328 | 0.431 |
| KG | 0.045 | 1.296 | 0.531 | 0.643 |

KG exhibits not only the largest mean ($\mu_{KG}$ = 0.53 m) but also the highest standard deviation ($\sigma_{KG}$ = 0.38 m), indicating the broadest distribution of offset values. While the standard deviation for PP and BS are comparable (0.26 m and 0.28 m, respectively), the mean and RMS offset are considerably smaller for BS. As for the synthetic example, BS provides the best estimation of electrode movements. With a RMS offset of 0.43 m, using this technique true electrode positions can be recovered with an accuracy better than 10% of the initial electrode spacing, despite very complex landslide movements. This is in the same order of magnitude than resistivity data based approaches to track electrode movements, as introduced in Wilkinson et al., 2010, Wilkinson et al., 2015. We have to note however, that this offset might still introduce slight artefacts in the resulting resistivity models, e.g., 10% electrode misplacement may cause 10% to 20% error in the apparent resistivity (Zhou and Dahlin, 2003, Szalai et al., 2008, Wilkinson et al., 2010).

The weak performance of KG may be explained by the small number of reference points (45 markers) forming the sample data set for defining the experimental variogram to fit the data. Although studies on the synthetic example showed that a minimum of 30 points was necessary to obtain a coherent variogram, the higher complexity of a real landslide would require more sample points to obtain a better estimation of the landslide movements.

Also for the real example non-smooth interpolators, such as natural and nearest neighbour, have been tested, but showed poorer performance. This can be attributed to the features, which would cause a step-like change in movement pattern (e.g., fissures), being of smaller scale than the marker separation. Hence, their effect on the movement dynamics is negligible and a smooth interpolator superior, as it represents the slope scale landslide dynamics.

## 4.3. Effect on 3D inverse modelling

As shown in the inverse modelling of the synthetic data, wrong electrode positions inevitably result in artefacts in the resistivity models, which are likely to mask true resistivity changes caused by, e.g., varying moisture content. Here we will show the changes caused by electrode movement and true resistivity changes from a baseline data set in February 2012 to a measurement in February 2013, covering a period over which large movements occurred. For the latter comparison we assume that the climatic circumstances, e.g., temperatures, are similar and therefore that the resistivity distributions are comparable. The data quality of the two data sets is similar and reasonably good, with 92.07% and 91.99% of the data, respectively, having reciprocal errors smaller than 5%. Data with reciprocal errors above 5% were removed from the data set before inversion.

The data were inverted using a smoothness-constrained least-squares inversion method, employing a L2-norm on the model and an L1-norm on the data (Loke and Barker, 1996). The forward problem was solved using a finite-element method, allowing the topography to be integrated into the model. The model comprises 4320 cells, with 9 cells in the $x$-, 32 in $y$-, and 15 cells in $z$-directions. Fig. 9b shows the inverted resistivity model for the 2012 data set.
Fig. 11 presents cross-sections through the 3D models (the location of the section is shown as blue line in Fig. 9a) for February 2012 and February 2013, employing the set of known electrode positions, and data from February 2013, which have been inverted using the electrode positions from 2012 and estimated positions for 2013 using BS (Fig. 11c and d, respectively). The profile of 2013 gives a clear indication of the WMF sliding over the SSF, and shows the boundary between SSF and RMF. The effects of using misplaced electrodes in the data inversion can be seen in Fig. 11c, where the SSF shows a clearly disturbed resistivity distribution compared to the resistivity model obtained from the true positions (Fig. 11b). The strongest artefacts caused by misplaced electrodes can be found in the zone of strong movements ($y$ = 35 m to 85 m) where the

resistivity is shown to increase in the near-surface of up to 35%. By using the locations estimated by the BS (Fig. 11d), the strongest distortions have been significantly reduced to an increase of only about 15%. This improved agreement with the resistivity model employing the true positions can also be seen by a higher correlation coefficient of $R = 0.924$ for the inversion using the BS positions compared to the one using the initial positions with $R = 0.712$, which also indicates that the corrected data shows significantly less artefacts. These results highlight that employing estimated electrode positions in the inversion of resistivity data can significantly reduce the effects of artefacts caused by landslide movement, with a reduction of up to 15% in the zone of strong movement and 2% to 5% in the remaining regions.
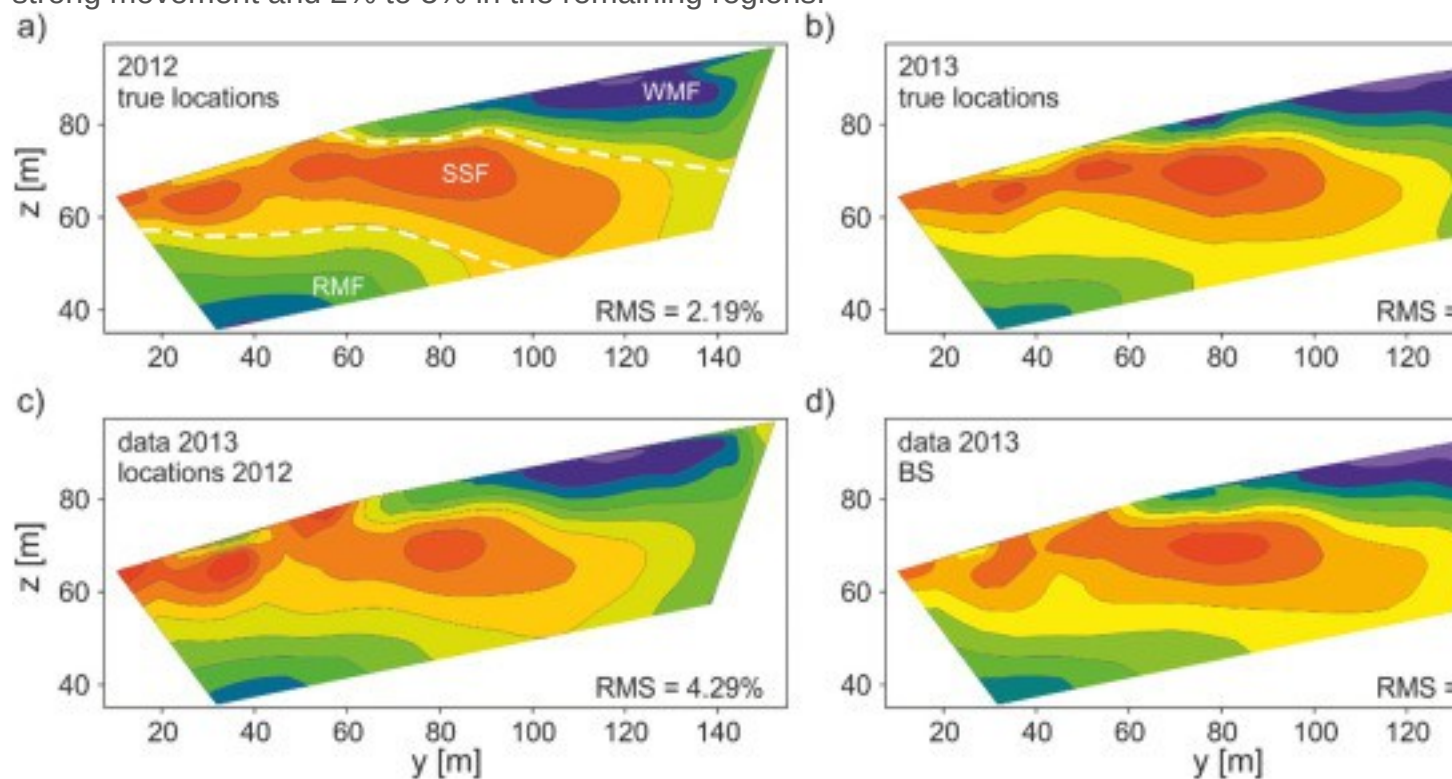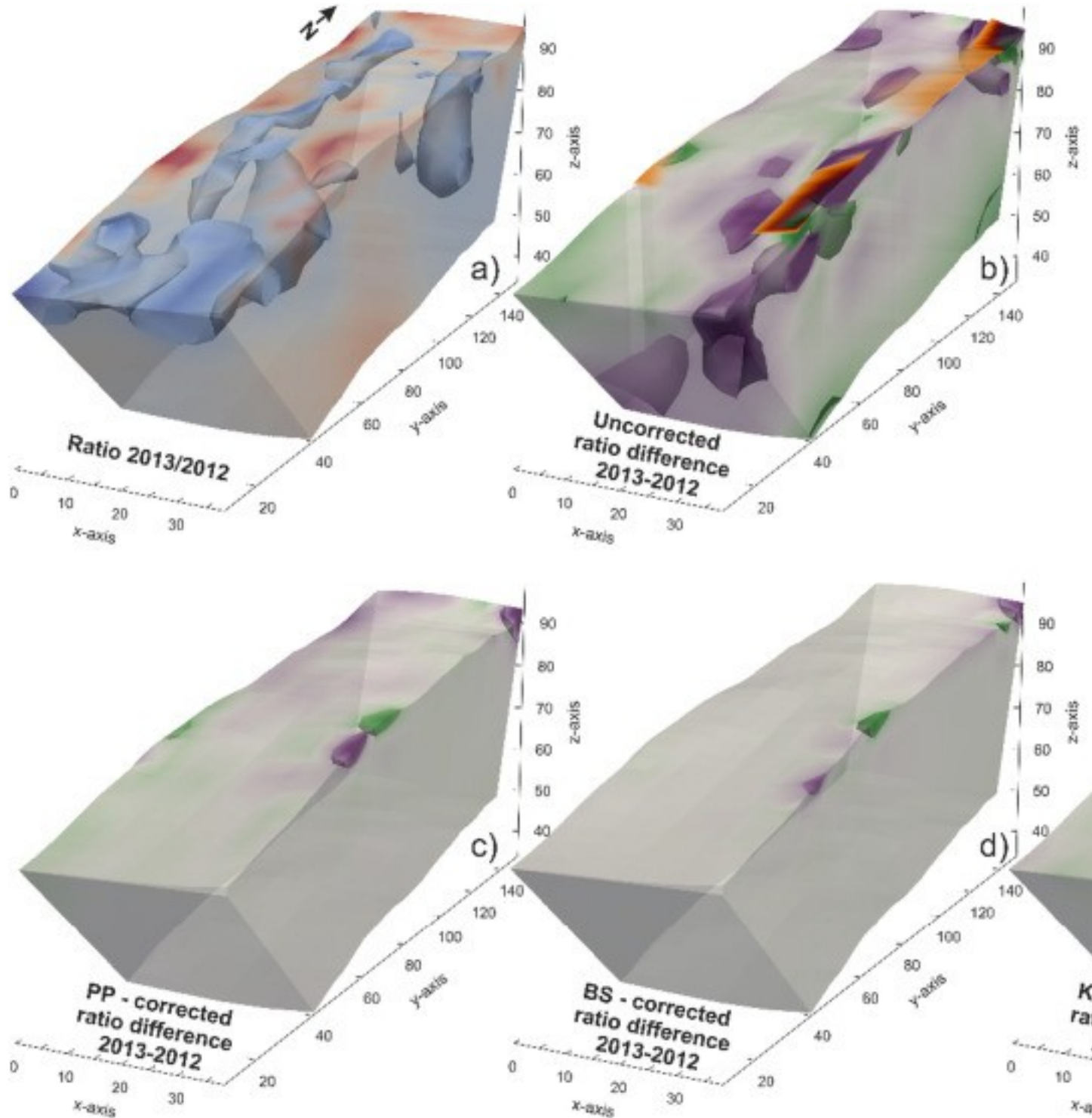


1. Download full-size image

Fig. 11. Cross-sections through the 3D resistivity models (location as shown in Fig. 9a) for different years and employing different electrode locations. a)–b) Resistivity model of February 2012 and 2013, respectively, employing correct electrode positions. c)–d) Resistivity models of data from February 2013; c) employing electrode locations of 2012; d) employing electrode positions estimated for 2013 using BS.

Using misplaced electrodes in the processing of ERT data, and of monitoring data in particular, will inevitably lead to misinterpretation of resistivity data. This is shown in Fig. 12, where resistivity ratios for data from 2013 to 2012, and the differences caused by misplaced electrodes are shown. Fig. 12a shows the "true" resistivity ratio,

indicating the area of the slip surface of the eastern lobe ($x > 30$ m, $40$ m $< y < 80$ m), the area just downslope of a rotational failure ($x > 25$ m, $100$ m $< y < 130$ m), and the near-surface area of the toe of the slope as having a lower resistivities than the previous year, thus higher moisture content. These observations are in agreement with other site observations.



a) Ratio 2013/2012

b) Uncorrected ratio difference 2013-2012

c) PP - corrected ratio difference 2013-2012

d) BS - corrected ratio difference 2013-2012

Fig. 12. a) Resistivity ratios between 2013 and 2012 employing "true" electrode locations. b)–e) Show ratio differences between true ratio and ratios employing b) uncorrected electrode locations, c) PP-corrected, d) BS-corrected, and e) KG-corrected electrode locations. Note that using PP and BS artefacts are considerably reduced.

Figs. 12 b)–e) show the difference in resistivity ratio between the ratios employing uncorrected or estimated electrode locations and the true ratio. These differences should be representative for the artefacts caused by misplaced electrodes only. In the uncorrected case, locations of large differences correlate with areas of large movements. Similarly to the synthetic example, in areas where electrodes move apart (45 m < $y$ < 80 m, and $y$ > 140 m) near-surface ratios increase; in areas where electrodes move together (35 < $y$ < 45 m, and 130 < $y$ < 140 m) near-surface ratios decrease, with the extent and amplitude of these features being determined by the amount of electrode movement. These near-surface artefacts (< 2 m) are underlain by deeper features of opposite polarity and smaller amplitude, reaching depths of up to 7 m. Near to the model boundaries, where ERT sensitivities are decreasing, these deeper artefacts may reach depths of up to 15 m.

Using estimated electrode locations reduces the amplitudes of these artefacts considerably. In case of PP and BS all deep artefacts are removed and amplitudes and spatial extent of the near-surface artefacts are reduced to an extent that they are virtually removed. The performance of these two techniques is highly comparable, with only small remaining ratio differences in areas of strongest movements, coinciding with locations of limited electrode movement recovery. As KG showed the worst performance of the three interpolators, larger ratio differences remain, which are not only restricted to the near-surface, but also appear in regions of low sensitivity at the lowermost part of the model.

The better agreement between true ratio and the one using the interpolated electrode positions can also be seen by a high correlation factor of $R_{BS}$ = 0.90, in contrast to $R$ = 0.11 for the uncorrected case. This shows that by correcting for electrode movement misinterpretation of ERT in particular, but all kind of spatial data in general, can be minimised.

## 5. Conclusions

Soil movements will affect the interpretation of any sensor whose reading is location dependent deployed on an active, moving landslide as long as those movements are not recognized and corrected for. We have introduced a methodology to estimate

movements for a large set of points or grids, for which direct movement monitoring is not feasible or possible, from a smaller, sparsely distributed set of reference points, both in space and time, and have compared three different interpolation techniques. The first interpolation technique is a piecewise planar interpolation, which is based upon planar transformations and calculates the electrode position by the changing vectors spanned between three neighbouring markers. The biharmonic spline or multiquadric interpolation scheme is a global-interpolation method using linear combinations of biharmonic Green's functions centred on each reference point, minimising the curvature of the interpolator. The third approach uses the widely-employed geostatistical interpolation technique of kriging. Applied to a synthetic example resembling realistic landslide movements, we showed that the three techniques were able of recovering non-linear movements to about 3% of the initial electrode spacing. It was also highlighted that the KG, due to its statistical nature, requires a sufficient number of sample points (i.e., more than 30) to correctly estimate movements. The smallest offset between true and estimated positions were obtained using the BS in the synthetic example, negligible larger values were found for PP. Both methods showed slightly larger discrepancies between true and estimated positions near the upper and lower model boundaries. The importance of correcting data for landslide movement was shown with a synthetic ERT example, which showed strong artefacts (± 80% of the initial model resistivity) when using uncorrected positions. These artefacts were virtually removed when using corrected electrode positions. The significance of this problem for a real data example has been shown in the case of a 3D ERT monitoring setup on an active landslide. Here, the sample data set was formed by a time series of real-time kinematic GPS measurements of marker points representing the soil movements, which were then interpolated to a grid of electrode locations. Applying the three techniques to this data set highlighted again the superior performance of PP and BS, which obtained comparable results, with BS showing the smallest mean and RMS offsets. On this landslide with highly heterogeneous movement characteristics, it was possible to recover true electrode positions to about 10% of the initial electrode spacing. It was also shown that the spatial and temporal sampling of the soil movements by repeated measurements of marker positions will affect the results. Inverse modelling of resistivity data employing non-corrected and corrected electrode locations, using the introduced interpolation techniques, highlighted the importance of adjusting sensor positions on landslides for movements. While important features (i.e., zones of high moisture content indicating areas of movement) were masked by artefacts in the uncorrected case, artefacts in these regions were virtually removed using the estimated electrode

positions. Although the results showed that electrode positions can only be recovered to a certain degree of accuracy using the methods introduced in this paper, we were able to show that this degree is sufficient to reduce artefacts and misinterpretation of resistivity data by using a simple approach of monitoring small sets of reference points. The proposed methodology for correcting electrode positions for landslide movements should therefore form an important part in the data processing scheme of ERT monitoring data. These methods are time and cost-effective and allow for robust interpretation of data obtained from any sensors that are subjected to movements and offer the opportunity to interpolate movements to a landslide scale rather than interpreting movements on a point scale only.

## Acknowledgements

## References

Archie, 1942

G.E. Archie**The electrical resistivity log as an aid in determining some reservoir characteristics**

Pet. Trans. AIME, 146 (1942), pp. 54-62

CrossRefView Record in Scopus

Chambers et al., 2011

J.E. Chambers, P.B. Wilkinson, O. Kuras, *et al.***Three-dimensional geophysical anatomy of an active landslide in Lias Group mudrocks, Cleveland Basin, UK**

Geomorphology, 125 (2011), pp. 472-484, 10.1016/j.geomorph.2010.09.017

ArticleDownload PDFView Record in Scopus

Chambers et al., 2014

J.E. Chambers, D.A. Gunn, P.B. Wilkinson, *et al.***4D electrical resistivity tomography monitoring of soil moisture dynamics in an operational railway embankment**

Near Surf. Geophys. (2014), pp. 61-72

View Record in Scopus

Chilès and Delfiner, 2012

J.-P. Chilès, P. Delfiner**Kriging**

Geostatistics, John Wiley & Sons, Inc. (2012), pp. 147-237

CrossRefView Record in Scopus

Corsini et al., 2005

A. Corsini, A. Pasuto, M. Soldati, A. Zannoni**Field monitoring of the Corvara landslide (Dolomites, Italy) and its relevance for hazard assessment**

Geomorphology, 66 (2005), pp. 149-165, 10.1016/j.geomorph.2004.09.012

ArticleDownload PDFView Record in Scopus

Dai et al., 2002

F. Dai, C. Lee, Y. Ngai**Landslide risk assessment and management: an overview**

Eng. Geol., 64 (2002), pp. 65-87

ArticleDownload PDFView Record in Scopus

Dijkstra and Dixon, 2010

T.a. Dijkstra, N. Dixon**Climate change and slope stability in the UK: challenges and approaches**

Q. J. Eng. Geol. Hydrogeol., 43 (2010), pp. 371-385, 10.1144/1470-9236/09-036

CrossRefView Record in Scopus

Dixon et al., 2010

N. Dixon, M. Spriggs, P. Meldrum, R. Ogilvy**Development of a low cost acoustic emission early warning system for slope instability**

A.L. Williams (Ed.), Geol. Act. Proc. 11th IAEG Congr, CRC Press, Auckland, New Zealand (2010), pp. 1803-1810

View Record in Scopus

Gance et al., 2014

J. Gance, J.-P. Malet, T. Dewez, J. Travelletti**Target detection and tracking of moving objects for characterizing landslide displacements from time-lapse terrestrial optical images**

Eng. Geol., 172 (2014), pp. 26-40, 10.1016/j.enggeo.2014.01.003

ArticleDownload PDFView Record in Scopus

Gaunt et al., 1980

G.D. Gaunt, H.C. Ivimey-Cook, I.E. Penn, B.M. Cox**Mesozoic Rocks Proved by IGS Boreholes in the Humber and Acklam Areas**

Institute of Geological Studies, Nottingham (1980)

Gharibi and Bentley, 2005

M. Gharibi, L. Bentley**Resolution of 3-D electrical resistivity images from inversions of 2-D orthogonal lines**

J. Environ. Eng. Geophys., 10 (2005), pp. 339-349

CrossRefView Record in Scopus

Gunn et al., 2013

D.A. Gunn, J.E. Chambers, P.R.N. Hobbs, *et al.***Rapid observations to guide the design of systems for long-term monitoring of a complex landslide in the Upper Lias clays of North Yorkshire, UK**
Q. J. Eng. Geol. Hydrogeol., 46 (2013), pp. 323-336, 10.1144/qjegh2011-028
CrossRefView Record in Scopus

Gunn et al., 2014

D.A. Gunn, J.E. Chambers, S. Uhlemann, *et al.***Moisture monitoring in clay embankments using electrical resistivity tomography**
Constr. Build Mater., 92 (2014), pp. 82-94, 10.1016/j.conbuildmat.2014.06.007

Hardy, 1971

R. Hardy**Multiquadric equations of topography and other irregular surfaces**
J. Geophys. Res., 76 (1971), pp. 1905-1915
CrossRef

Hardy, 1990

R. Hardy**Theory and applications of the multiquadric–biharmonic method 20 years of discovery 1968–1988**
Comput. Math. Appl., 19 (1990), pp. 163-208
ArticleDownload PDFView Record in Scopus

Hobbs et al., 2012

P.R.N. Hobbs, D.C. Entwisle, K.J. Northmore, *et al.***Engineering Geology of British Rocks and Soils**
Lias Group (2012)

Jomard et al., 20

H. Jomard, T. Lebourg, S. Binet, *et al.***Characterization of an internal slope movement structure by hydrogeophysical surveying**

Terra Nova, 19 (2007), pp. 48-57, [10.1111/j.1365-3121.2006.00712.x](#)

[CrossRef](#)[View Record in Scopus](#)

Jongmans and G

D. Jongmans, S. Garambois**Geophysical investigation of landslides: a review**

Bull. Soc. Géol. Fr., 33 (2007), pp. 101-112

[CrossRef](#)[View Record in Scopus](#)

Lebourg et al., 2

T. Lebourg, M. Hernandez, S. Zerathe, *et al.***Landslides triggered factors analysed by time lapse electrical survey and multidimensional statistical approach**

Eng. Geol., 114 (2010), pp. 238-250, [10.1016/j.enggeo.2010.05.001](#)

[Article](#)[Download PDF](#)[View Record in Scopus](#)

Loke and Barker

M. Loke, R. Barker**Practical techniques for 3D resistivity surveys and data inversion**

Geophys. Prospect., 44 (1996), pp. 499-523

[CrossRef](#)[View Record in Scopus](#)

Matheron, 1971

G. Matheron**The Theory of Regionalized Variables and Its Applications**

(1971), p. 212

[View Record in Scopus](#)

Merritt et al., 201

A.J. Merritt, J.E. Chambers, W. Murphy, *et al.***3D ground model development for an active landslide in Lias mudrocks using geophysical, remote sensing and geotechnical methods**

Landslides, 11 (2013), pp. 537-550, [10.1007/s10346-013-0409-1](#)

Mora et al., 2003

P. Mora, P. Baldi, G. Casula, *et al.***Global positioning systems and digital photogrammetry for the monitoring of mass movements: application to the Ca' di Malta landslide (northern Apennines, Italy)**

Eng. Geol., 68 (2003), pp. 103-121, [10.1016/S0013-7952(02)00200-4](#)

[Article](#)[Download PDF](#)[View Record in Scopus](#)

Ogilvy et al., 200

R.D. Ogilvy, P.I. Meldrum, O. Kuras, *et al.***Automated monitoring of coastal aquifers with electrical resistivity tomography**

Near Surf. Geophys., 7 (2009), pp. 367-375

[View Record in Scopus](#)

Oldenborger et a

G.A. Oldenborger, P.S. Routh, M.D. Knoll**Sensitivity of electrical resistivity tomography data to electrode position errors**

Geophys. J. Int., 163 (2005), pp. 1-9

[CrossRef](#)[View Record in Scopus](#)

Sandwell, 1987

D. Sandwell**Biharmonic spline interpolation of GEOS-3 and SEASAT altimeter data**
Geophys. Res. Lett., 14 (1987), pp. 139-142
[CrossRef](#)[View Record in Scopus](#)

Supper et al., 20

R. Supper, D. Ottowitz, B. Jochum, *et al.***Geoelectrical monitoring: an innovative method to supplement landslide surveillance and early warning**
Near Surf. Geophys., 12 (2014), pp. 133-150, [10.3997/1873-0604.2013060](#)
[View Record in Scopus](#)

Szalai et al., 200

S. Szalai, A. Koppán, L. Szarka**Effect of positional inaccuracies on multielectrode results**
Acta Geodaet. Geophys. Hung., 43 (2008), pp. 33-42, [10.1556/AGeod.43.2008.1.3](#)
[CrossRef](#)[View Record in Scopus](#)

Uhlemann et al.,

S. Uhlemann, A. Smith, J. Chambers, *et al.***Assessment of ground-based monitoring techniques applied to landslide investigations**
Geomorphology (2015)
(in revision)

Wilkinson et al.,

P.B. Wilkinson, J.E. Chambers, P.I. Meldrum, *et al.***Predicting the movements of permanently installed electrodes on an active landslide using time-lapse geoelectrical resistivity data only**
Geophys. J. Int., 183 (2010), pp. 543-556
[CrossRef](#)[View Record in Scopus](#)

Wilkinson et al.,

P.B. Wilkinson, S. Uhlemann, J.E. Chambers, *et al.***Development and testing of displacement inversion to track electrode movements on 3-D electrical resistivity tomography monitoring grids**
Geophys. J. Int., 200 (2015), pp. 1566-1581, [10.1093/gji/ggu483](#)
[CrossRef](#)[View Record in Scopus](#)

Zhou and Dahlin

B. Zhou, T. Dahlin**Properties and effects of measurement errors on 2D resistivity imaging surveying**
Near Surf. Geophys., 1 (2003), pp. 105-117
[View Record in Scopus](#)